Composite Structures 246 (2020) 112379

Contents lists available at ScienceDirect

Composite Structures

journal homepage: www.elsevier.com/locate/compstruct

Post-buckling failure studies on quasi-isotropic CFRP panels under positive and negative in-plane shear loading

Naresh Reddy Kolanu[a], Gangadharan Raju[b], Ramji M[a,*]

[a] Engineering Optics Lab, Department of Mechanical and Aerospace Engineering, IIT Hyderabad, India
[b] NDT & E Lab, Department of Mechanical and Aerospace Engineering, IIT Hyderabad, India

ARTICLE INFO

Keywords:
Positive shear
Negative shear
Post-buckling
Digital image correlation
Acoustic emission
Progressive damage model

ABSTRACT

The shear buckling performance of a flat laminated composite structure depends on various factors like the nature of the applied load, lamina orthotropy, stacking sequence and the support boundary conditions. The emphasis of the current work is to decipher the effect of the direction of applied shear on the post-buckling response and failure of a quasi-isotropic carbon CFRP panel. A comprehensive experimental test campaign involving 3D-digital image correlation (DIC), acoustic emission (AE) and strain gaging techniques are used to capture the post-buckling deformation and the associated failure mechanisms in the CFRP test panels under positive and negative shear load. Further, a generic finite element based progressive damage model involving 3D Hashin's failure criteria in conjunction with the cohesive zone model is developed in Abaqus software for simulating the intra and inter-laminar damages in the quasi-isotropic laminate and later compared with the experimental results. The effect of positive and negative shear on the post-buckling response and the associated damage modes are investigated in detail. The outcome of the current investigations reveals that the direction of the shear load has a definite impact on the post-buckling response and failure behavior of the CFRP test panels.

1. Introduction

Advanced fiber-reinforced composite materials are widely used in modern aerospace applications owing to their superior mechanical properties and structural tailorability options. The primary load-bearing composite structures in aircraft are thin-walled and susceptible to buckling when subjected to in-plane loading conditions like compression, shear, or combined loads. Buckling is an important design constraint in the design of aircraft structures and they are generally designed to operate below the buckling load. However, platelike composite structures exhibit stable post-buckling behavior, and new design methodologies are being explored for enhancing the weight savings by allowing the aircraft structural designers to work in the post-buckling regime. The degree of post-buckling allowed depends on the type of structure, and the aerodynamic constraints often dictate them. Empennage and wing covers are mostly held buckling resistant, on the other hand, fuselage panels, ribs and spars of wing box allow post-buckling designs. But the post-buckling collapse of laminated composite panels is still not clearly understood, especially under shear. The challenge is to solve the nonlinear problem comprising of large transverse deformation (geometrical nonlinearity) and the evolution of various damages (material nonlinearity) in the post-buckling regime. It requires sophisticated experimental and numerical tools to understand the post-buckling response and their interaction with the damage modes in composite laminates. In this work, the post-buckling behavior and collapse of composite laminate under in-plane shear load are studied using both experimental and numerical techniques.

A review of the early investigations on the shear buckling performance of composite panels is presented in Refs. [1–7]. Researchers in the late 1980's demonstrated the development of analytical and numerical methods for understanding the buckling behavior of the composite panels [8–13]. Since the 1990's, increasing number of works have been reported on the post-buckling studies of composite panels under various loading conditions [14–17]. But, the overall survey shows that the investigation of composite panels under in-plane shear has attracted less attention compared to compression loading. Recent years have witnessed emerging studies on the post-buckling analysis of composite structures subjected to in-plane shear loading [18–21]. Kumar et al. [18,21] numerically studied the effects of cut-out shape, size and direction of shear load on buckling and post-buckling behavior, failure loads and failure characteristics of quasi-isotropic panels. They have reported that the cut-out shape, direction of applied shear load and the composite layup have a considerable effect on the strength and failure characteristics of the test panels. Raju *et al.* [22] studied the

* Corresponding author at: Department of Mechanical and Aerospace Engineering, IIT Hyderabad, Kandi, Sangareddy 502285, Telangana, India.
E-mail addresses: me13m15p000006@iith.ac.in (N.R. Kolanu), gangadharanr@iith.ac.in (G. Raju), ramji_mano@iith.ac.in (R. M).

https://doi.org/10.1016/j.compstruct.2020.112379
Received 14 December 2019; Received in revised form 23 March 2020; Accepted 14 April 2020
Available online 20 April 2020
0263-8223/ © 2020 Elsevier Ltd. All rights reserved.

buckling, post-buckling behavior of variable angle tow (VAT) composite panels under in-plane positive and negative shear loads and compared their performance with the straight fiber composites. The numerical results are computed using the differential quadrature method and then compared with the finite element results. However, these preliminary studies [18–22] are analytical/numerical in nature. These theoretical investigations invariably prompt questions regarding the validation of the results and requires experimental verification. However, in literature, only a limited number of experimental investigations are available related to the shear buckling behavior of laminated composites [23–26]. There are no experimental studies available on studying the effect of the direction of applied shear load on the buckling and post-buckling characteristics of composite panels.

Therefore in the present work, the structural performance of a quasi-isotropic CFRP laminate under positive and negative shear loading up to the collapse has been studied in detail to understand the stability behavior and their associated failure mechanisms. The current work use non-contact techniques like digital image correlation (DIC), Air-coupled ultrasonics and infrared thermography (IR) [27,28] and other in situ damage monitoring techniques like acoustic emission (AE) [29–34] for better understanding of the structural behavior and complex damage characteristics of composite laminates. In addition, finite element modeling is carried out to enhance our understanding of the post-buckling response and the associated failure mechanisms of a quasi-isotropic CFRP panel under in-plane shear loading.

2. Experimental investigations

2.1. Details of the test panel geometry and boundary conditions

The test panels used in the present study are fabricated in–house using vacuum bagging technique. The laminates are made up of unidirectional (UD) carbon fiber reinforcements (HinFab® 200 gsm-Supplied by Hindoostan Mills Ltd.) embedded in an epoxy matrix (Araldite® CY-230). Additional details related to the fabrication of the test panels are given in Ref.[35]. The geometry of the test panels, along with the prescribed boundary conditions, is illustrated in Fig. 1. The test panel used in the present study is a quasi-isotropic $[45/90/-45/0]_s$ panel of square geometry. The nominal thickness of the panel after curing is measured to be 1.8 mm with an individual-ply thickness of 0.225 mm. An in–house, custom made picture frame setup is fabricated and used for applying the shear load on the CFRP test panels. Diagonal tension/compression load applied at one corner of the picture frame with the opposite corner being fixed results in positive/negative shear load, respectively, on the test panel. The schematic of the positive and negative shear load application on the test panel is shown in Fig. 2. Details of the picture frame loading fixture are given in Ref.[35].

2.2. Details of experimental setup and procedure

In the current study, MTS Landmark® servo-hydraulic fatigue testing machine of capacity 100 kN is used for loading the test panels. The shear load is applied to the test panels in the displacement control mode at a rate of 0.5 mm/min. Fig. 3 shows the typical experimental setup involving a test frame and various other real-time monitoring techniques. The deformation of the test panel is monitored using the DIC whole-field imaging technique for acquiring the displacement and strain field measurements. AE technique is involved for real-time in situ monitoring of the various damage modes in the test panel. The details related to the 3D-DIC system, surface preparation for whole-field deformation measurements, and other real-time damage monitoring sensors are discussed in detail in Ref.[35].

However, for supporting the DIC strain estimates, conventional strain measurement gages (350 ohms electrical strain gages) are also used for capturing the strains in the critical regions of the test panels (Ref.Fig. 4)). In addition to the above techniques, four wide-band piezoelectric AE sensors are bonded to the test panel for acquiring the AE signals corresponding to the various damages encountered in the test panel. The physical locations of the AE sensors are illustrated in the Fig. 4. Prior to the test, the AE sensors are calibrated by performing a standard pencil lead break test. A sub-threshold value of 40 dB is maintained to filter the noise signals generated by the load frame and the loading fixture. During the experiment, the elastic waves generated by the initiation and evolution of the various damage modes are acquired by the AE sensors. The AE signals are further enhanced using pre-amplifiers (Gain 40 dB) and stored on a computer using a data acquisition card. Later, the characteristics of the AE signals are analyzed to identify and classify the various damage modes experienced by the test panel.

2.3. Details of non-destructive testing (NDT) and fractography equipment

Apart from the in situ AE damage monitoring, the fractured test panels are also inspected using air-coupled ultrasonic testing (ACUT) and infrared pulse thermography (IPT) for the post-test damage assessments. The equipment used in the current study for the NDT and fractographic inspections are shown in Fig. 5. ACUT is a non-contact ultrasonic measurement method used for imaging the damages in the

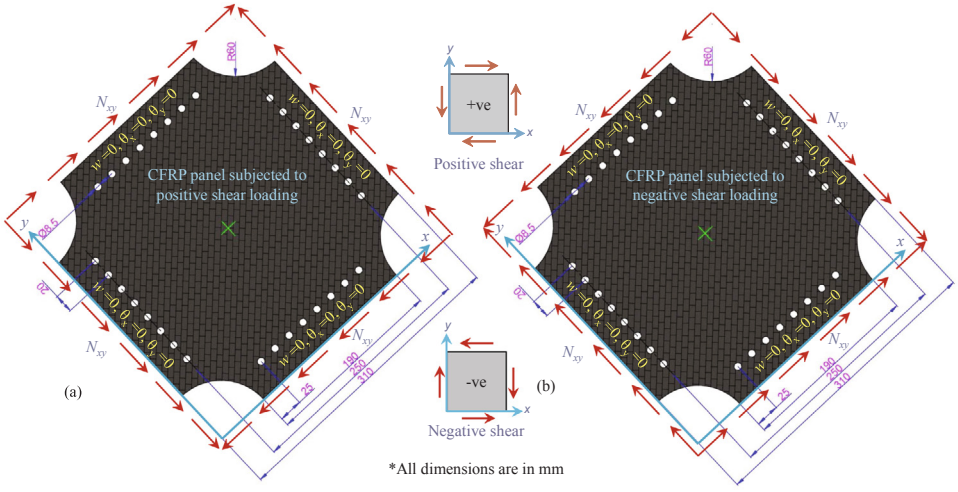

Fig. 1. Schematic of the CFRP test panel showing its geometry and boundary conditions (a) Positive shear load (b) negative shear load.

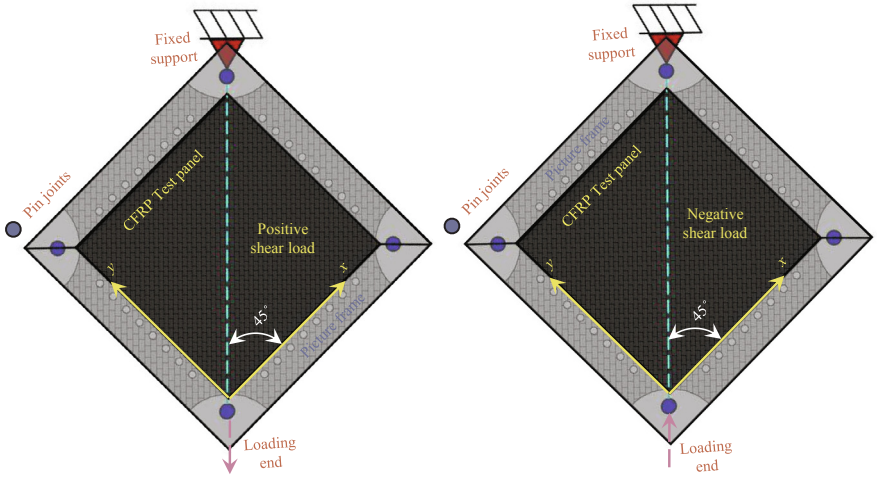

Fig. 2. Schematic of the shear load application (a) Positive shear load (b) negative shear load.

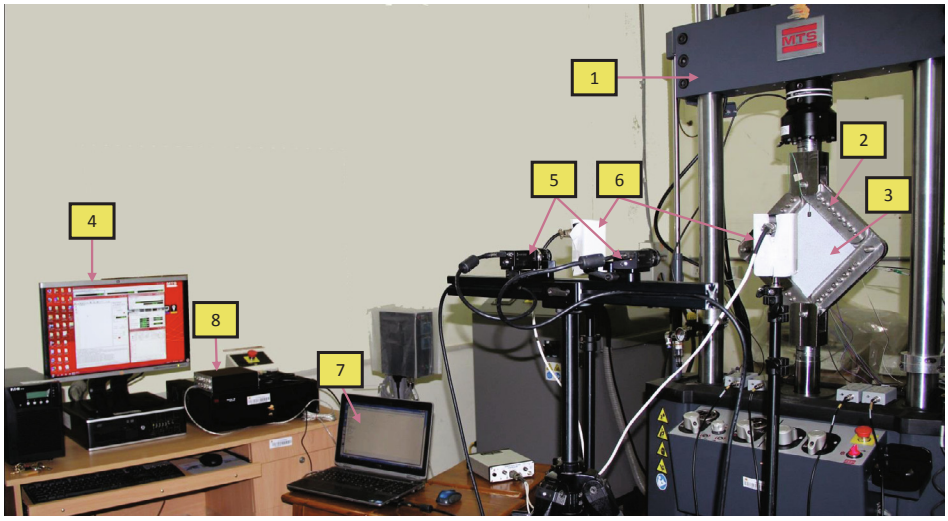

(1) MTS Load frame (2) Picture frame setup (3) CFRP test panel (4) MTS user interface (5) CCD cameras (6) LED light source
(7) Image grabbing computer (8) NI data acquisition card

Fig. 3. Typical experimental setup involving real-time deformation and damage monitoring techniques.

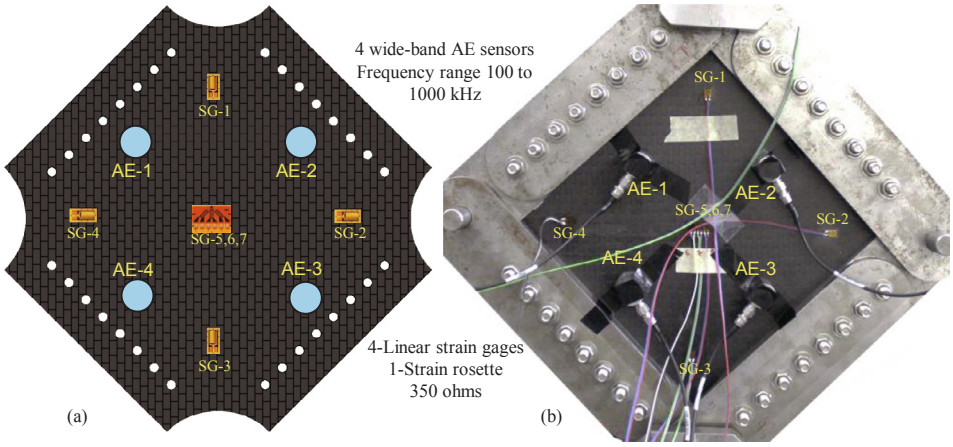

Fig. 4. The locations of the bonded strain gages and piezoelectric AE sensors (a) schematic (b) actual panel.

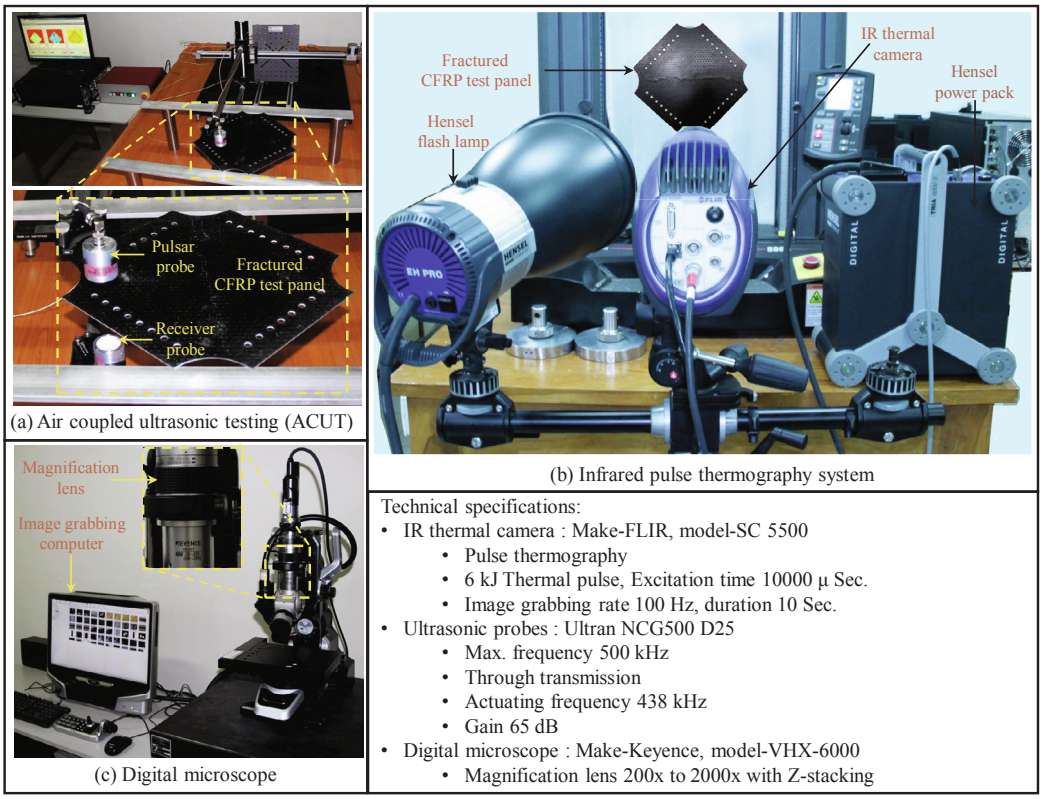

Fig. 5. Photograph of the experimental setup used for NDT and fractography studies (a) air-coupled ultrasonics (b) infrared thermography (c) digital microscope.

panel. It typically consists of an ultrasonic pulser-receiver, a data acquisition card, and a computer for post-processing of ultrasonic signals. (See Fig. 5(a)). Here in the current study, the ACUT inspections are performed in through-transmission mode. The frequency of the air-coupled probes (ULTRAN NCG500-D25) used in the current study is 500 kHz. The effective air gap between the test panel and the probes is maintained as 20 mm.

For the qualitative comparison of the damage assessments made by the ACUT method, the damaged test panels are also inspected using the pulse thermography technique. IPT consists of a flash lamp, power generator/power pack, IR camera, and computer for processing of thermal images. High energy pulses generated by a flash lamp are used to heat the test panel. Further, the energy required for creating the high energy pulses is provided by the voltage power pack and the IR camera is used for measuring the surface temperature distribution. (See Fig. 5(b)). In the present study, a high energy thermal pulse of 6 kJ energy is excited for about ten milliseconds and the sequential thermal images of the test panel are acquired at a rate of 100 Hz. A total of 1000 thermal images are captured over a period of 10 s. More technical details related to the AUCT and IPT inspections are provided in the Fig. 5. Moreover, for ascertaining the various damages manifested in the test panels, a detailed fractography study is carried out using a digital microscope (See Fig. 5(c)). The specimens extracted from the fractured zones are prepared for the microscopic observations. Further, images are acquired at different magnifications for ascertaining the presence of various damages in the test panels.

3. Numerical investigations

3.1. Details of the finite element model

Fig. 6 shows the finite element (FE) model of the shear test panels used in the current study. In the present study, the laminae in the test panel are modeled using the solid brick elements (C3D8R) with enhanced hourglass stiffness. While the interfaces between each lamina, are modeled using cohesive elements (COH3D8, 0.001 mm thick). A uniform mesh size of 2 mm is used to discretize the FE model, which is based on the results obtained from the mesh convergence study. The number of elements along the thickness direction is equal to 8, which equals one element per lamina. The aspect ratio of the solid elements is maintained well within the limits of the guidelines (⩽10) to avoid the numerical instability issues. A total of 1,32,540 number of elements have resulted in the FE model with 1,44,400 number of nodes.

The material orientation is assigned as per the stacking sequence to the individual lamina by defining a local element coordinate system. Further, the nodes on the panel edges are coupled to the top and bottom ends by creating two master nodes, as shown in Fig. 6(a). Only rotation is allowed at the four corners of the test model. The top end of the FE model is constrained by fixing all degrees of freedom (DOF). The load is applied at the bottom end such that it is allowed to move only in loading direction and the remaining DOF's are constrained. The compression (tension) displacement at the loading end results in an in-plane positive (negative) shear load on the test model.

The post-buckling analysis starts with an initial Eigen buckling analysis for extracting the critical buckling loads and mode shapes. Later, the Eigen-mode shapes obtained from the buckling analysis are used as scaled imperfection functions (5% of skin thickness) for the subsequent non-linear post-buckling analysis. The degradation in the material due to intra-laminar (fiber and matrix failures) damages is simulated by employing a 3D-Hashin based PDM and the inter-laminar (delaminations) damages are simulated using cohesive elements. Material properties used in the current PDM are evaluated in–house from the standard coupon tests (Ref. Tables 1 and 2). However, the in situ strength effects are not taken into account as the average thickness of the individual ply is 0.22 mm [36].

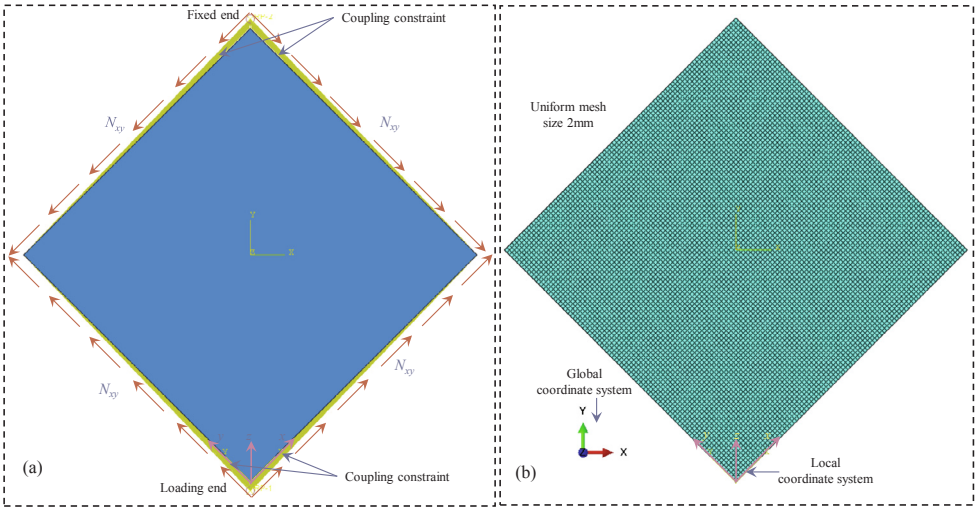

Fig. 6. Details of the FE model (a) schematic with boundary conditions (b) meshed FE model.

Table 1
Material properties of the CFRP laminate [37]

Carbon/Epoxy composite (HinFab® UD fabric and Araldite® CY230 resin)		
Stiffness and strength properties	Units	Avg. value with Std.dev.
Longitudinal modulus	E_{11} (GPa)	105.68 ± 1.2
Transverse modulus	E_{22} (GPa)	4.64 ± 0.3
In-plane shear modulus	G_{12} (GPa)	3.34 ± 0.2
In-plane Poisson's ratio	ν_{12}	0.36 ± 0.02
Longitudinal tensile strength	X_T (MPa)	1280 ± 80
Transverse tensile strength	Y_T (MPa)	20 ± 4
Longitudinal compressive strength	X_C (MPa)	500 ± 45
Transverse compressive strength	Y_C (MPa)	50.26 ± 4.6
In-plane shear strength	S_{12} (MPa)	42 ± 0.6
Out-of-plane Poisson's ratio	ν_{23}	0.49
Out-of-plane modulus	G_{23} (GPa)	1.55
Laminate fracture toughness	Units	Avg. value with Std.dev.
Fiber tension	G_{ft} (N/mm)	140 ± 15
Fiber compression	G_{fc} (N/mm)	102 ± 6
Matrix tension	G_{mt} (N/mm)	0.32 ± 0.03
Matrix shear	G_{ms} (N/mm)	0.68 ± 0.05

Table 2
Cohesive properties for epoxy (Araldite®-CY230).

inter-laminar properties (Epoxy-CY230)	Mode-I	Mode-II	Mode-III
Interfacial strength (MPa)	18	14	14
Fracture toughness (N/mm)	0.32	0.68	0.68
Interface stiffness (MPa/mm)	10^6	10^6	10^6

3.2. Intra-laminar progressive damage modeling

For simulating the intra-laminar damage initiation, a user-defined material subroutine (UMAT) based on Hashin's damage criteria is developed in the Abaqus FE software. Further, a set of gradual stiffness degradation rules are employed for simulating the damage evolution within the laminae.

3.2.1. Intra-laminar damage initiation criteria

The post-buckling behavior of the CFRP composite panels under shear loading exhibits large in-plane and out-of-plane deformations. This leads to the intra-laminar matrix failures in the in-plane and out-of-plane directions. However, the fiber mostly fails under in-plane compression and tension. Therefore, the Hashin based damage initiation model used in this work contemplate seven different damage initiation criteria namely, fiber tension (F_{ft}), fiber compression (F_{fc}), in-plane matrix tension (F_{imt}), in-plane matrix compression (F_{imc}), out-of-plane matrix tension (F_{omt}), out-of-plane matrix compression (F_{omc}) and fiber–matrix shear-out (F_{fms}). The expressions for the seven damage initiation criteria are given as.

Fiber tension failure F_{ft} when $\epsilon_1 > 0$

$$F_{ft} = \sqrt{\left(\frac{\epsilon_1}{X_T/C_{11}}\right)^2 + \left(\frac{\gamma_{12}}{S_{12}/C_{44}}\right)^2 + \left(\frac{\gamma_{13}}{S_{13}/C_{55}}\right)^2} \quad (1)$$

Fiber compression failure F_{fc} when $\epsilon_1 < 0$

$$F_{fc} = \sqrt{\left(\frac{\epsilon_1}{X_C/C_{11}}\right)^2} \quad (2)$$

In-plane matrix tension failure F_{imt} when $\epsilon_2 > 0$

$$F_{imt} = \sqrt{\left(\frac{\epsilon_2}{Y_T/C_{22}}\right)^2 + \left(\frac{\gamma_{12}}{S_{12}/C_{44}}\right)^2 + \left(\frac{\gamma_{23}}{S_{23}/C_{66}}\right)^2} \quad (3)$$

In-plane matrix compression failure F_{imc} when $\epsilon_2 < 0$

$$F_{imc} = \sqrt{\left(\frac{\epsilon_2}{Y_C/C_{22}}\right)^2 + \left(\frac{\gamma_{12}}{S_{12}/C_{44}}\right)^2 + \left(\frac{\gamma_{23}}{S_{23}/C_{66}}\right)^2} \quad (4)$$

Out-of-plane matrix tension failure F_{omt} when $\epsilon_3 > 0$

$$F_{omt} = \sqrt{\left(\frac{\epsilon_3}{Z_T/C_{33}}\right)^2 + \left(\frac{\gamma_{13}}{S_{13}/C_{55}}\right)^2 + \left(\frac{\gamma_{23}}{S_{23}/C_{66}}\right)^2} \quad (5)$$

Out-of-plane matrix compression failure F_{omc} when $\epsilon_3 < 0$

$$F_{omc} = \sqrt{\left(\frac{\epsilon_3}{Z_C/C_{33}}\right)^2 + \left(\frac{\gamma_{13}}{S_{13}/C_{55}}\right)^2 + \left(\frac{\gamma_{23}}{S_{23}/C_{66}}\right)^2} \quad (6)$$

Fiber-matrix shear failure F_{fms} when $\epsilon_1 < 0$

$$F_{fms} = \sqrt{\left(\frac{\epsilon_1}{X_C/C_{11}}\right)^2 + \left(\frac{\gamma_{12}}{S_{12}/C_{44}}\right)^2 + \left(\frac{\gamma_{13}}{S_{13}/C_{55}}\right)^2} \quad (7)$$

In the Eqns. (1–7), the term C_{ij} (i,j = 1,2,….6) represents the components of stiffness tensor, ϵ_i (i = 1,2,3) are the normal strains and γ_{ij} (i = 1,2,3; i ≠ j) are the shear strains. X_T and X_C represent tensile and compressive strengths along the fiber direction, Y_T and Y_C represent tensile and compressive strengths in the transverse direction, Z_T and Z_C represent tensile and compressive strengths in the out-of-plane direction respectively. Shear strength of the laminate are denoted by S_{12}, S_{13} and S_{23}.

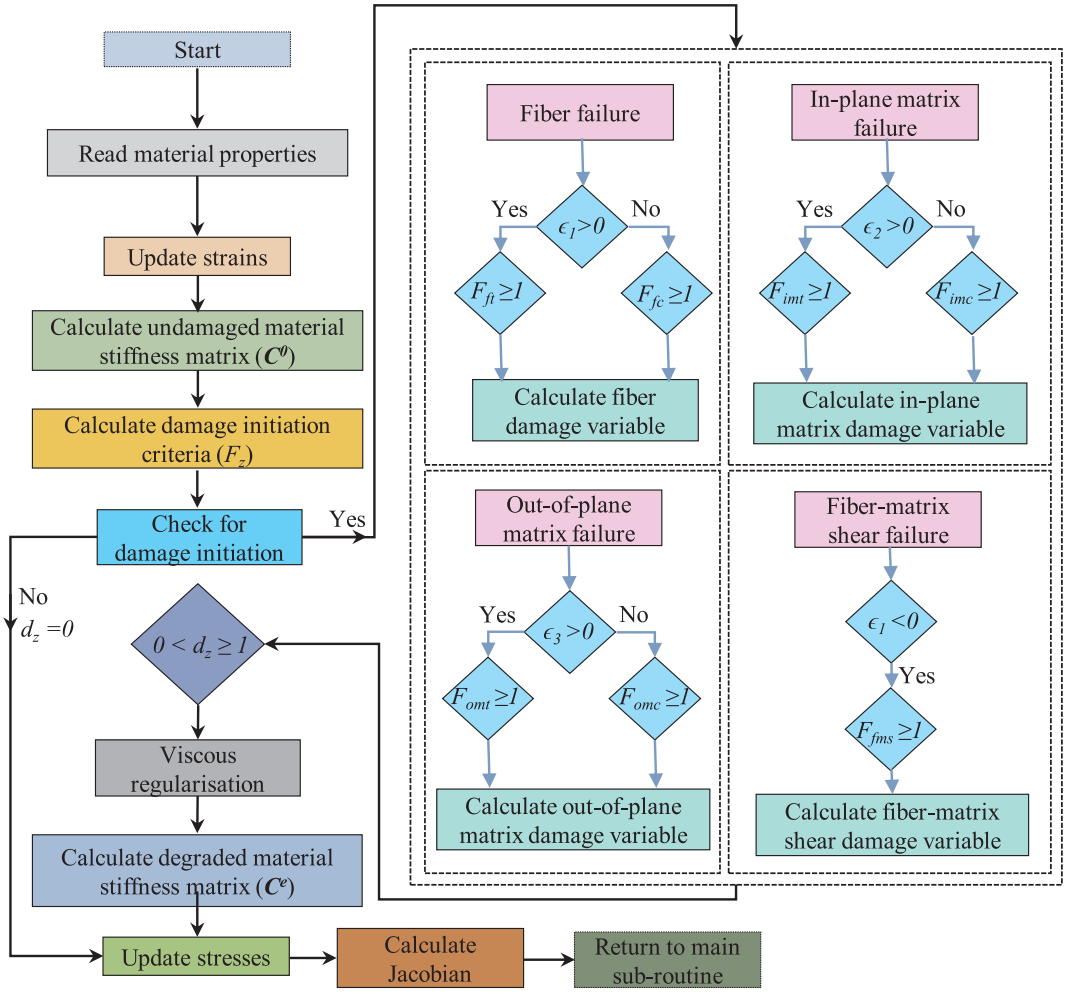

Fig. 7. Flow chart for the progressive damage modeling using UMAT.

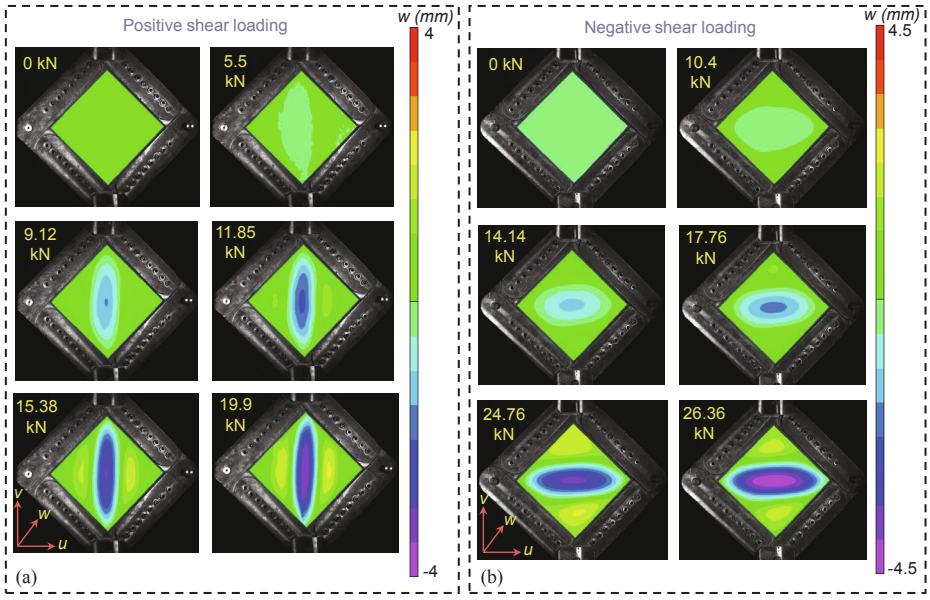

Fig. 8. Evolution of buckling mode shapes with in-plane shear loading (a) positive shear (b) negative shear.

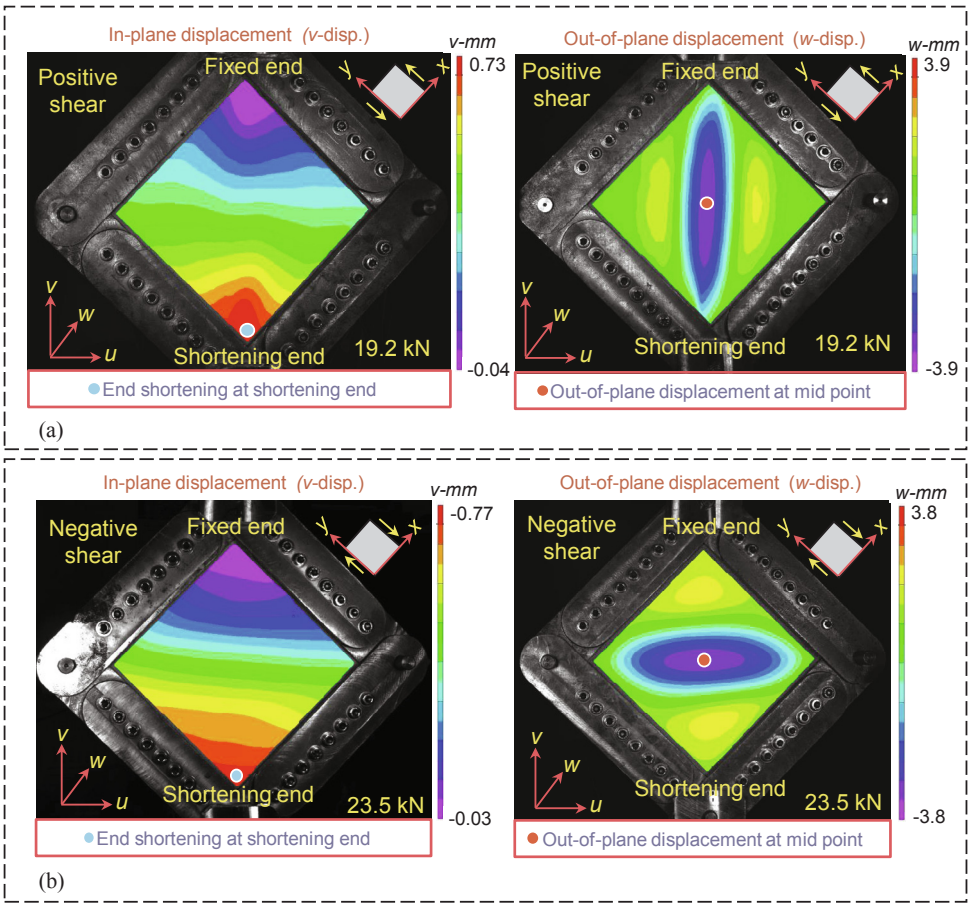

Fig. 9. Whole-field in-plane (v) and out-of-plane (w) displacement contours for (a) positive shear loading (b) negative shear loading.

3.2.2. *Intra-laminar damage evolution criteria*

The PDM algorithm for simulating the damage initiation and evolution in the FE model is shown in Fig. 7. The damage status of each element is checked at the gauss points. Once the damage initiation criteria are satisfied, certain selective stiffness properties of the associated elements are degraded in a gradual manner. As the post-buckling response is governed by the bending behavior of the CFRP laminates, the choice of damage variable (d_z) is made from the bending studies available in the literature [38]. The damage variable used in the current study is an exponential function given by,

$$d_z = 1 - \frac{1}{F_z} exp\left(\frac{C_{ij}\,\epsilon_i^2(1-F_z)L^C}{G_z}\right) \tag{8}$$

where L^C represents the characteristic length of the element, F_z are the damage initiation criteria, and G_z is the fracture energy of the fiber or matrix dissipated during the damage evolution.

The solution convergence of the current PDM is improved by adopting viscous regularization schemes [39]. After the initiation of damage, the associated effective stiffness tensor $\mathbf{C^e}$ with degraded stiffness is evaluated (Ref. Eq. (9)). The stiffness coefficients are quadratic functions of the damage variable and are expressed as,

$$\mathbf{C^e} = \begin{bmatrix} C_{11}^e & C_{12}^e & C_{13}^e & 0 & 0 & 0 \\ & C_{22}^e & C_{23}^e & 0 & 0 & 0 \\ & & C_{33}^e & 0 & 0 & 0 \\ & symmetric & & C_{44}^e & 0 & 0 \\ & & & & C_{55}^e & 0 \\ & & & & & C_{66}^e \end{bmatrix} \tag{9}$$

$$\begin{aligned} C_{11}^e &= (1-d_{ff})^2 C_{11} \\ C_{12}^e &= (1-d_{ff})(1-d_{imf}) C_{12} \\ C_{13}^e &= (1-d_{ff})(1-d_{omf}) C_{13} \\ C_{22}^e &= (1-d_{imf})^2 C_{22} \\ C_{23}^e &= (1-d_{imf})(1-d_{omf}) C_{23} \\ C_{33}^e &= (1-d_{omf})^2 C_{33} \\ C_{44}^e &= (1-d_{fms})^2 C_{44} \\ C_{55}^e &= (1-d_{ff})(1-d_{omf}) C_{55} \\ C_{66}^e &= (1-d_{imf})(1-d_{omf}) C_{66} \end{aligned} \tag{10}$$

In Eq. (10), the subscripts represents the different failure modes:*ff* for fiber failure in tension or compression, *imf* for in-plane matrix failure, *omf* for out-of-plane matrix failure and *fms* for fiber–matrix shear failure. After the evaluation of the degraded stiffness matrix, the stresses are updated as

$$\boldsymbol{\sigma} = \mathbf{C}\colon \boldsymbol{\epsilon} \begin{cases} \text{if } (0 < d_z \le 1) & \mathbf{C} = \mathbf{C^e} \\ \text{if } (d_z = 0) & \mathbf{C} = \mathbf{C^0} \end{cases} \tag{11}$$

Later, the tangent stiffness matrix (Jacobian) is evaluated using the expression

$$\frac{\partial \boldsymbol{\sigma}}{\partial \boldsymbol{\epsilon}} = \mathbf{C}^e + \frac{\partial \mathbf{C}^e}{\partial \boldsymbol{\epsilon}}\colon \boldsymbol{\epsilon} \tag{12}$$

To visualize the damage status of the elements, damage variables are stored as the solution dependent variables (SDV's) in the UMAT.

3.3. *Traction separation laws for cohesive elements*

The constitutive behavior for the cohesive elements is based on the

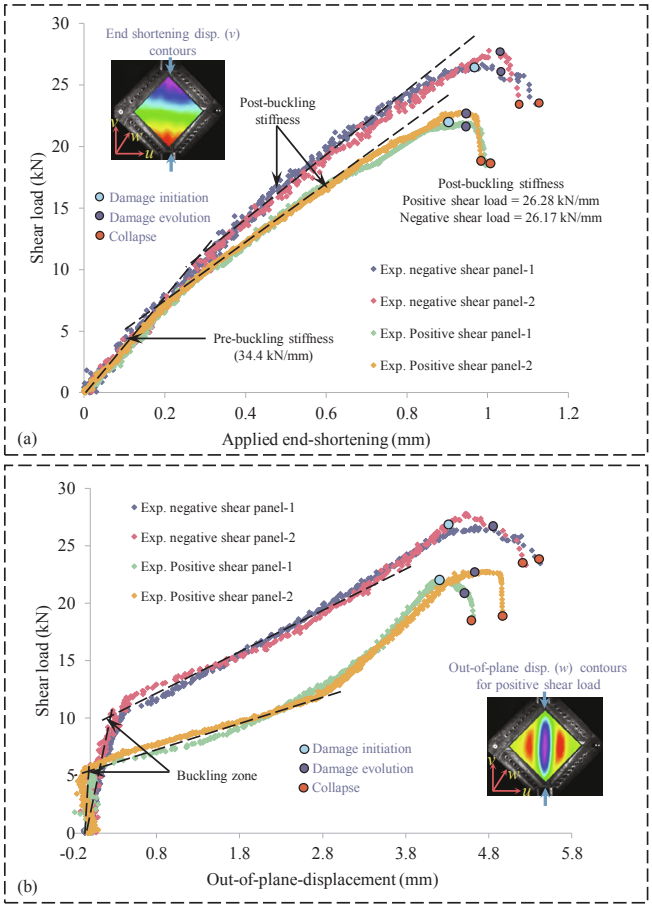

Fig. 10. Post-buckling performance of the CFRP composite panels under positive and negative in-plane shear loading (a) shear load vs. applied end-shortening (b) shear load vs. maximum out-of-plane displacement.

Table 3
Summary of post-buckling test results of CFRP composite panels under in-plane shear load.

Quantity	Positive shear load	Negative shear load
Shear buckling load (kN)	5.6	10
Maximum load (kN)	22.3	27.2
Maximum end-shortening (mm)	0.98	1.09
Maximum out-of-plane disp. (mm)	4.75	5.33

mixed-mode bi-linear traction-separation law. The onset of delamination is predicted using the quadratic stress criterion (Eq. (13)).

$$\left(\frac{\langle t_n \rangle}{t_n^0}\right)^2 + \left(\frac{t_s}{t_s^0}\right)^2 + \left(\frac{t_t}{t_t^0}\right)^2 = 1 \tag{13}$$

After the initiation of delamination, the softening behavior of the cohesive element is governed by bi-linear traction-separation law and expressed as,

$$K = \begin{cases} K_i^0 & \delta < \delta_i^0 \\ (1-d)K_i^0 & \delta_i^0 < \delta < \delta_i \text{.....} i = n,\ s,\ t \text{ normal and shear directions} \\ 0 & \delta > \delta_i \end{cases} \tag{14}$$

where d is a damage variable, which can vary between 0 and 1. Expression for the damage variable d in terms of the separation value is given as,

$$d = \frac{\delta_i(\delta - \delta_i^0)}{\delta(\delta_i - \delta_i^0)} \tag{15}$$

Further, the mixed mode criteria for damage evolution proposed by Benzeggagh and Kenane [40] is used in this work and is given by,

$$G^c = G_n^c + (G_s^c - G_n^c)\left(\frac{G_S}{G_T}\right)^\eta \tag{16}$$

where $G_S = G_s + G_t$, $G_T = G_n + G_s + G_t$ and η is the B-K material parameter evaluated from the mixed-mode bending experiments. Here, G_n, G_s and G_t are the strain energy release rate values corresponding to the normal and two orthogonal shear fracture modes respectively.

4. Results and discussions

4.1. Experimental results

In this section, the stability behavior and the collapse mechanisms exhibited by the CFRP composite test panels under positive and negative shear loading are presented. The whole-field deformations obtained using the 3D-DIC technique are analyzed for the prediction of the buckling modes, post-buckling response and the damage initiation sights. Further, the classification of the various damage modes encountered in the test panel is evaluated based on the AE parametric data. Further, the effect of shear direction on the buckling and post-buckling behavior and the associated damage mechanisms are also discussed.

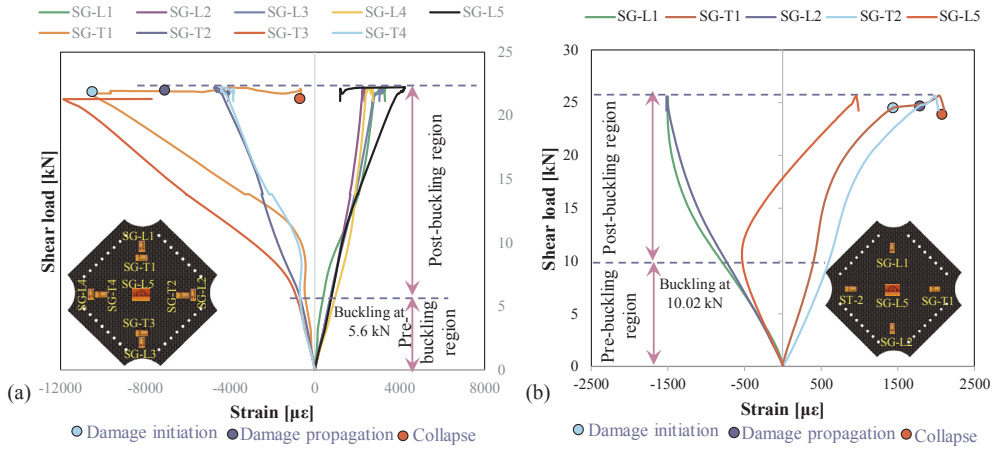

Fig. 11. Conventional strain measurements collected on the test panels under (a) positive shear (b) negative shear.

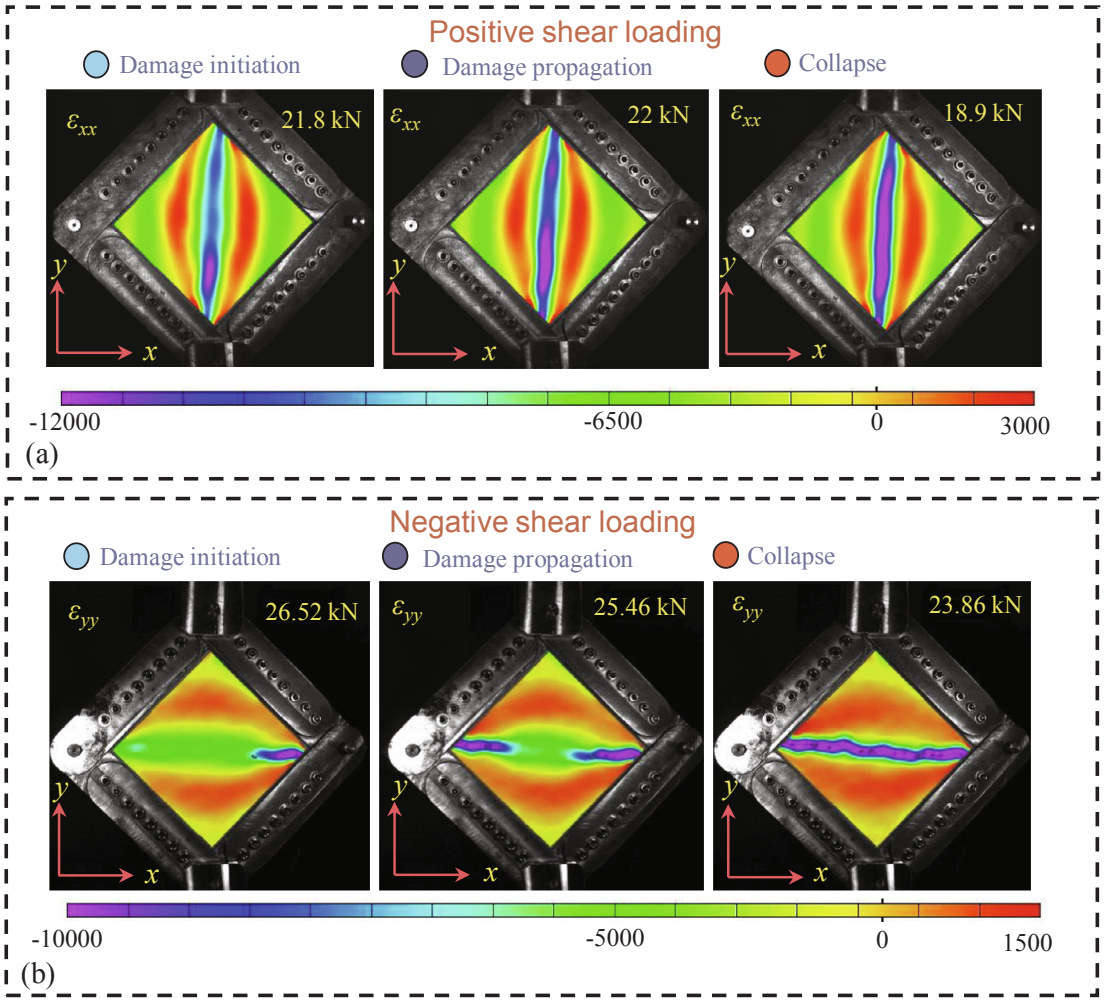

Fig. 12. Damage evolution obtained from 3D-DIC (a) positive shear (b) negative shear.

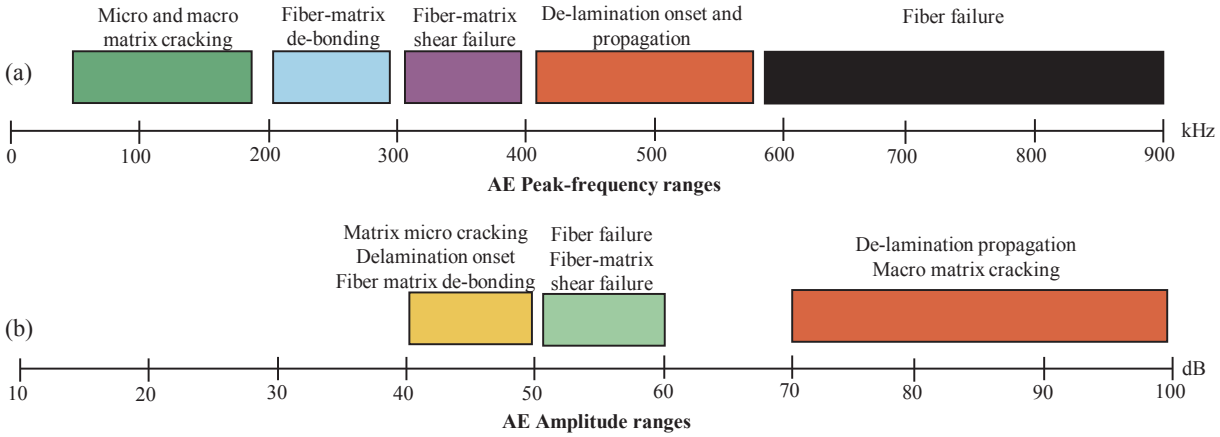

Fig. 13. Damage characterization based on AE parametric data (a) peak-frequency ranges (b) amplitude ranges.

4.1.1. Post-buckling performance of the test panels under positive and negative shear loads

The evolution of the buckling and post-buckling deformations with the variation of the shear load is depicted in Fig. 8. For the positive shear load case (See Fig. 8(a)), the buckling mode shape of the panel is observed at 5.5 kN load and the mode shape is maintained with further load increments. In the case of negative shear load (See Fig. 8(b)), the buckling mode deformation of the panel started at 10.4 kN load (almost double) and progressively deforms with further load increments. The DIC results show that buckling mode shapes are different for positive and negative shear loads. The mode shape seen for the positive shear load is half-waves aligned along the loading direction. But, for the negative shear load, the buckling mode shapes are half-waves aligned perpendicular to the loading direction.

For evaluating the post-buckling performance of the test panels, the end-shortening displacement and out-of-plane displacements are

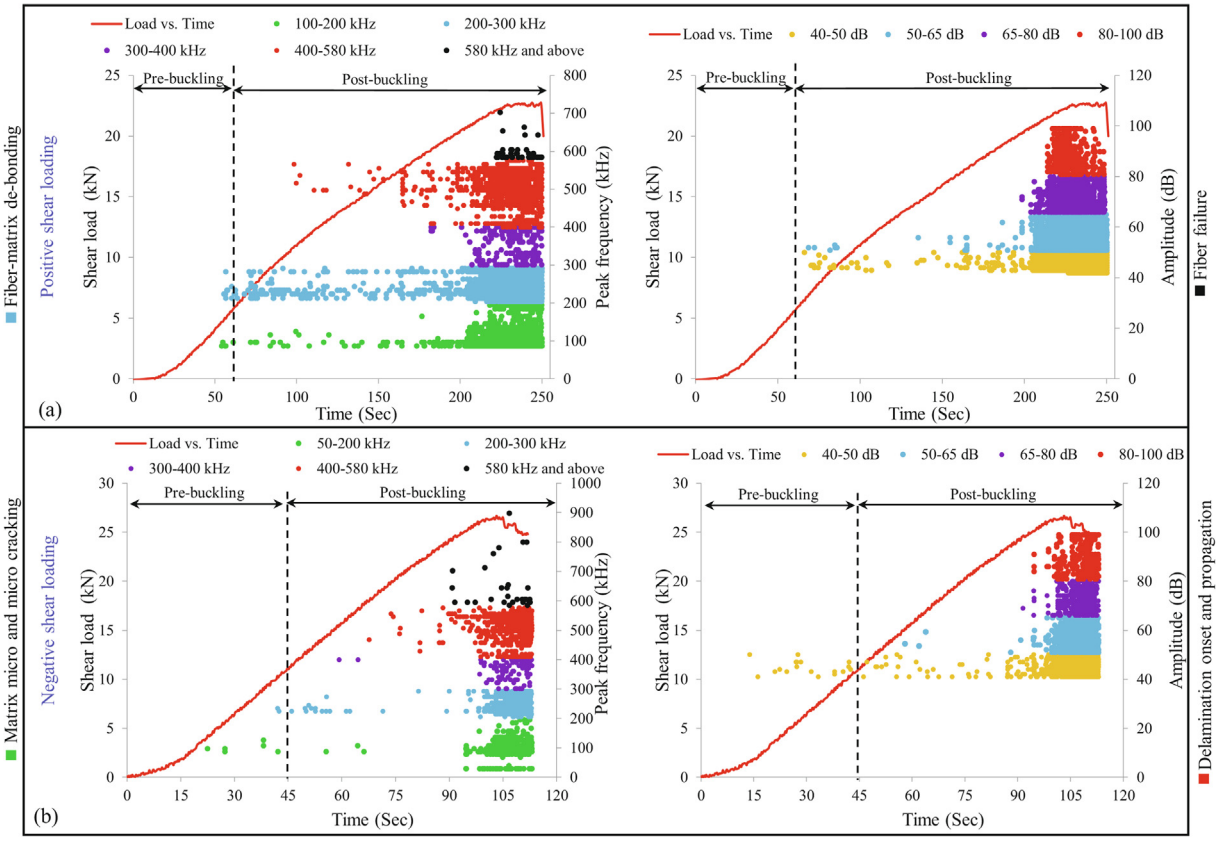

Fig. 14. AE peak frequency and amplitude plots (a) positive shear load (b) negative shear load.

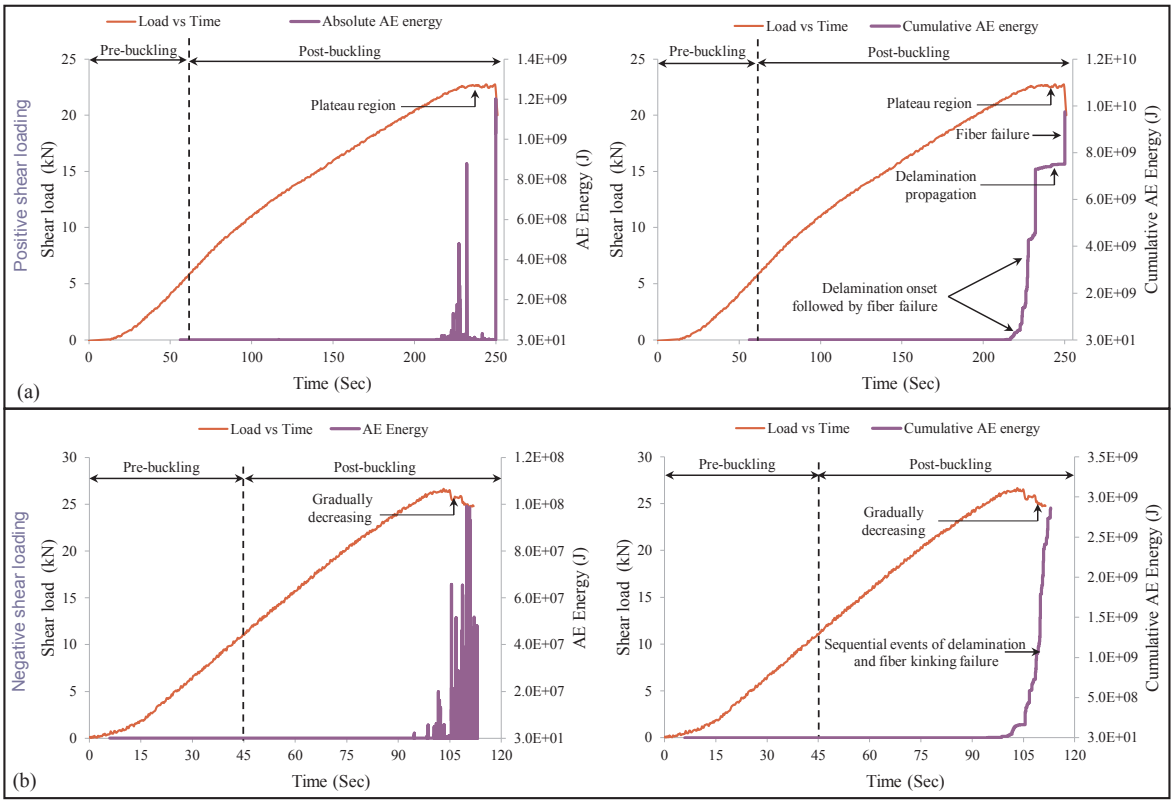

Fig. 15. AE energy plots (a) positive shear loading (b) negative shear loading.

Fig. 16. Damage signatures observed on post-fractured panels (a) positive shear (b) negative shear.

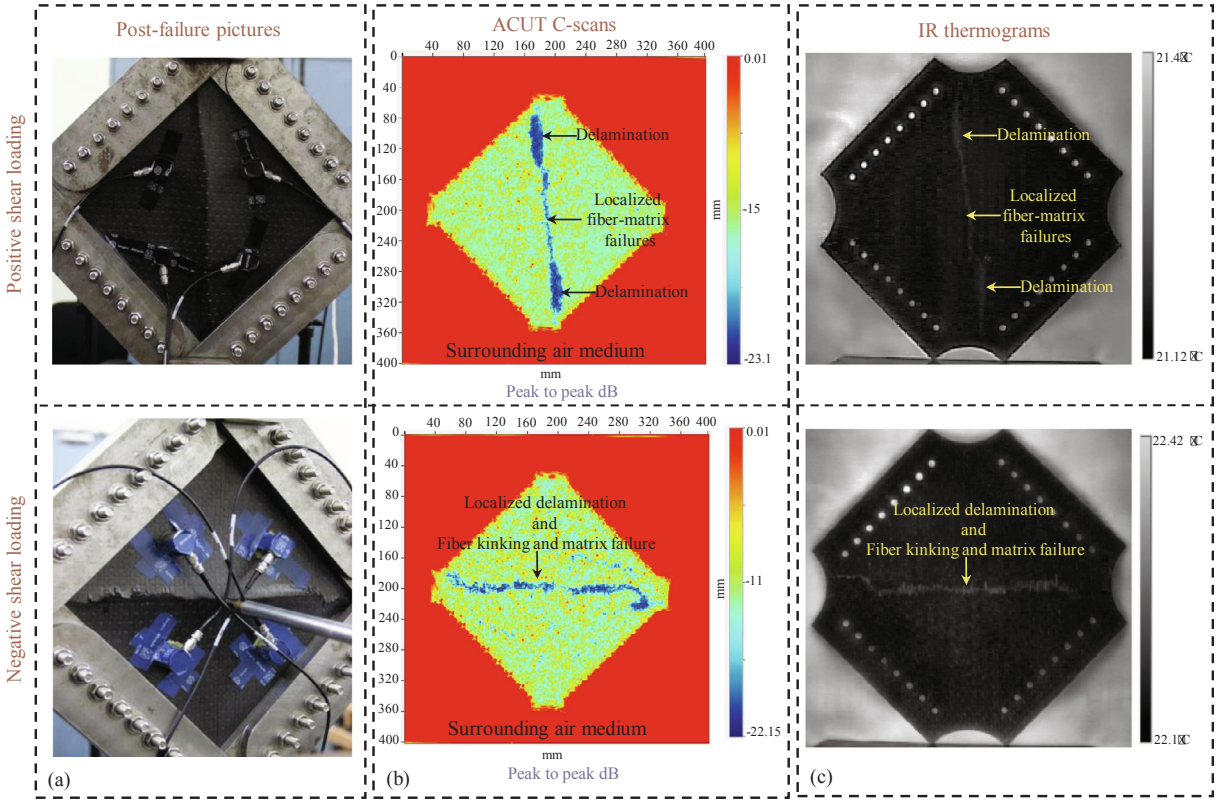

Fig. 17. Damages assessment based on NDT measurements (a) post-fracture pictures (b) ACUT C-scans (c) IR thermograms.

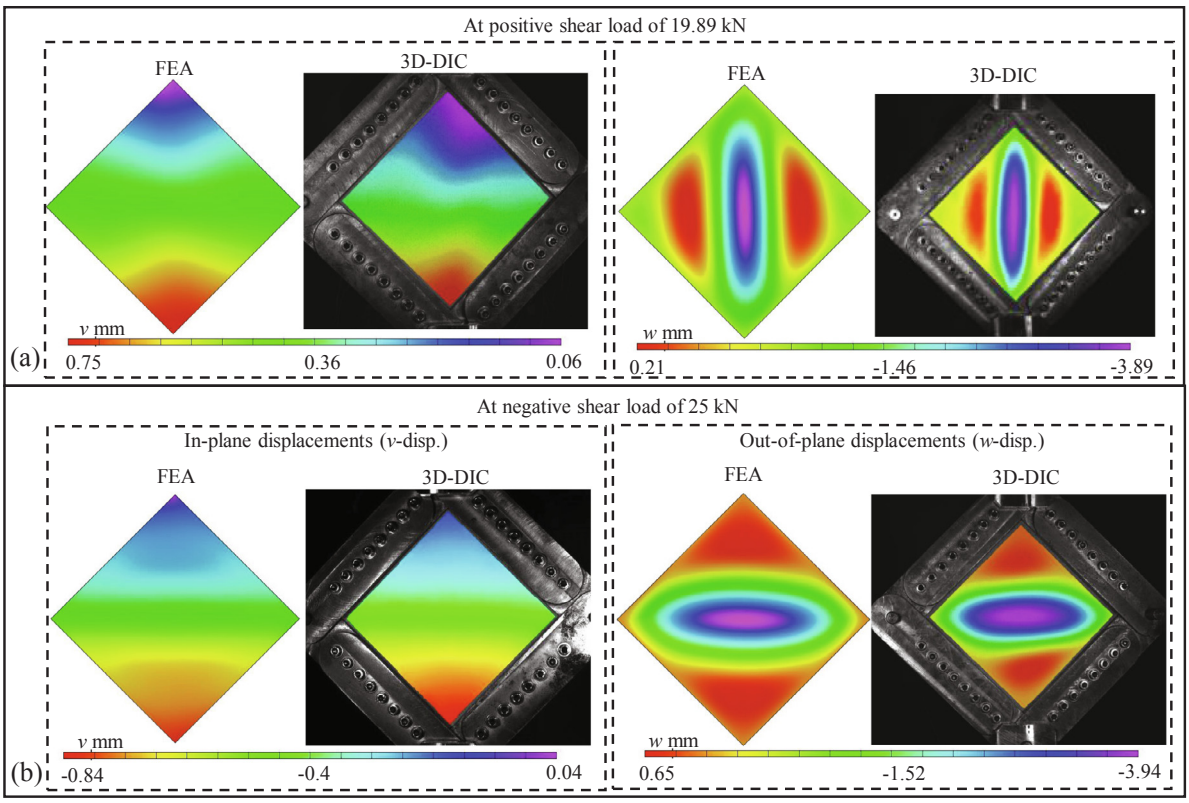

Fig. 18. Comparison of FEA and experimental (3D-DIC) results (a) positive shear (b) negative shear.

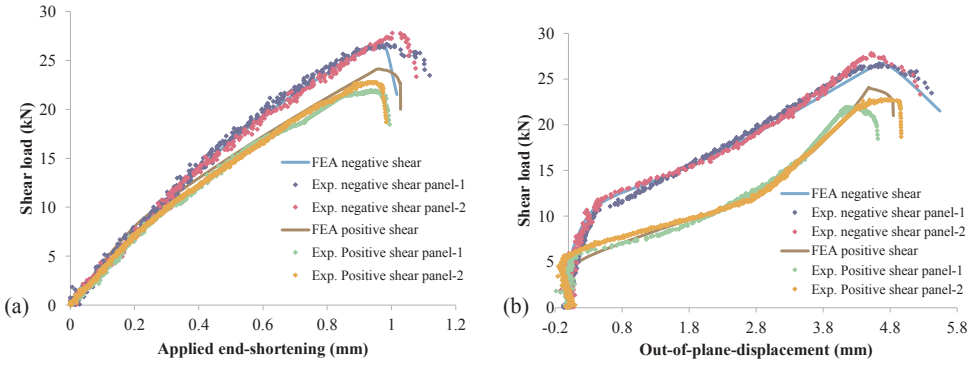

Fig. 19. Comparison of FEA and experimental (3D-DIC) load vs. displacement curves (a) end-shortening curves (b) out-of-plane displacement curves.

extracted from the whole-field data near the loading end and panel center, respectively (See Fig. 9)). The buckling and post-buckling responses exhibited by the CFRP test panels under positive and negative in-plane shear loading is shown in Fig. 10. It is observed that the test panel exhibits better buckling performance under negative shear compared to positive shear. The reason behind the improved performance under negative shear is attributed to the alignment of the compressive forces along the fiber direction.

The pre-buckling stiffness of the test panels is observed to the same under positive and negative shear loads. Test panels under positive and negative shear load exhibit a linear response in the load vs. end-shortening behavior till the onset of buckling with a pre-buckling stiffness of 34.4 kN/mm. The phenomenon of buckling is more appreciable from the load vs. out-of-plane displacement curves (See Fig. 10(b)). Although the CFRP panel under positive shear load has buckled early, the post-buckling response is observed to be approximately the same as that of the negative shear load case with a post-buckling stiffness of 26 kN/mm. The panels continue to take the load in the post-buckling stage and the average failure load under positive and negative shear loads are 22.3 kN and 27.2 kN, respectively. For confirming the repeatability of the experimental results, two test panels are tested for each case. A close match is observed between the two panels tested under identical loading conditions, which in-turn shows the repeatability of the experimental test procedure adopted in this work. The summary of the experimental buckling and post-buckling results are shown in Table 3.

The strain data at critical locations in the test panels are measured using the conventional strain gages. The response obtained from the axial strain gages with the applied positive and negative shear load is shown in Fig. 11(a) and (b), respectively. It is observed that the loads at which bifurcations occur are close to the buckling load value predicted from the DIC technique (Ref.Fig. 10(b). Under positive shear, the test panel experiences tension along the loading direction and compression in the transverse direction. Whereas, it is vice versa in the case of

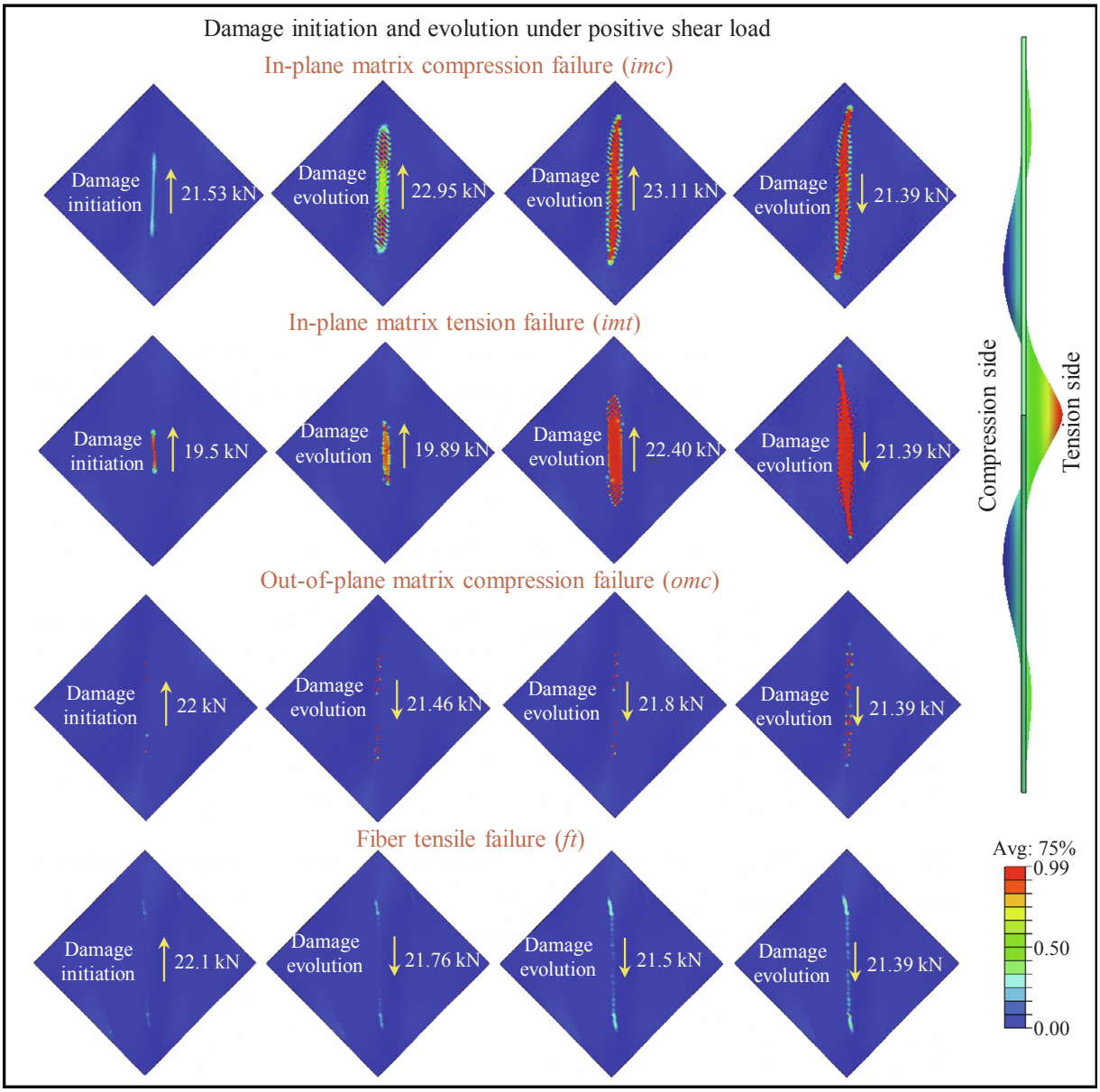

Fig. 20. Damage initiation and evolution simulated by the PDM under positive shear load.

negative shear. Therefore, in the case of positive shear the strain gages aligned along the loading direction (SG-L1, SG-L2, SG-L3, SG-L4, and SG-L5) show a tensile response (Ref.Fig. 11)) and the transverse strain gages (SG-T1, SG-T2, SG-T3, and SG-T4) which are perpendicular to the loading exhibit compressive state. However, in the case of negative shear, the resultant force along the loading direction is compressive. Therefore, the strain gages (SG-L1 and SG-L2), which are aligned along the loading experience compressive strains, and the transverse strain gages (SG-T1 and SG-T2) have experience tension.

4.1.2. Damage assessments obtained from DIC and AE techniques

The whole-field measurements from the DIC are used for studying the damage initiation and evolution zones in the test panels. Fig. 12(a) and (b) show the transverse (ε_{xx}) and longitudinal (ε_{yy}) strain maps at the three different stages of the damage (initiation, evolution, and collapse) for positive and negative shear, respectively. The damage initiates near the corners of the test panel, irrespective of the shear direction and propagate towards the center of the test panel. Under positive shear, the damage evolved from the longitudinal corners of the test panel and progress longitudinally towards the center. Whereas, under negative shear, damage initiates from the horizontal corners and propagate towards the center of the test panel.

Further, the parametric data obtained from the AE technique is used for identifying and classifying the various damages in the test panels. The characteristic AE parameter ranges used for damage classification in the present study are obtained from preliminary investigations carried out by the authors in their previous works, Ref. [41,35,37]. The peak-frequency and amplitude ranges obtained for the various damage modes involved in the CFRP test panel under positive and negative shear load are presented in Fig. 13.

The AE peak-frequency and amplitude plots associated with the damage events encountered in the test panels under positive and negative shear loads are shown in Fig. 14 (a) and (b), respectively. After the onset of buckling, AE events of low frequency and less energy content (micro-cracks) is observed (Ref. Fig. 14 and 15) and does not have any effect on the load response. Further, near the failure load, an increasing trend in the AE events is observed, which indicates more damage events in the test panel. The damage evolution is witnessed by continuous and sequential interactive events of intra-laminar (matrix cracking, fiber–matrix shear and fiber kinking) failures and inter-

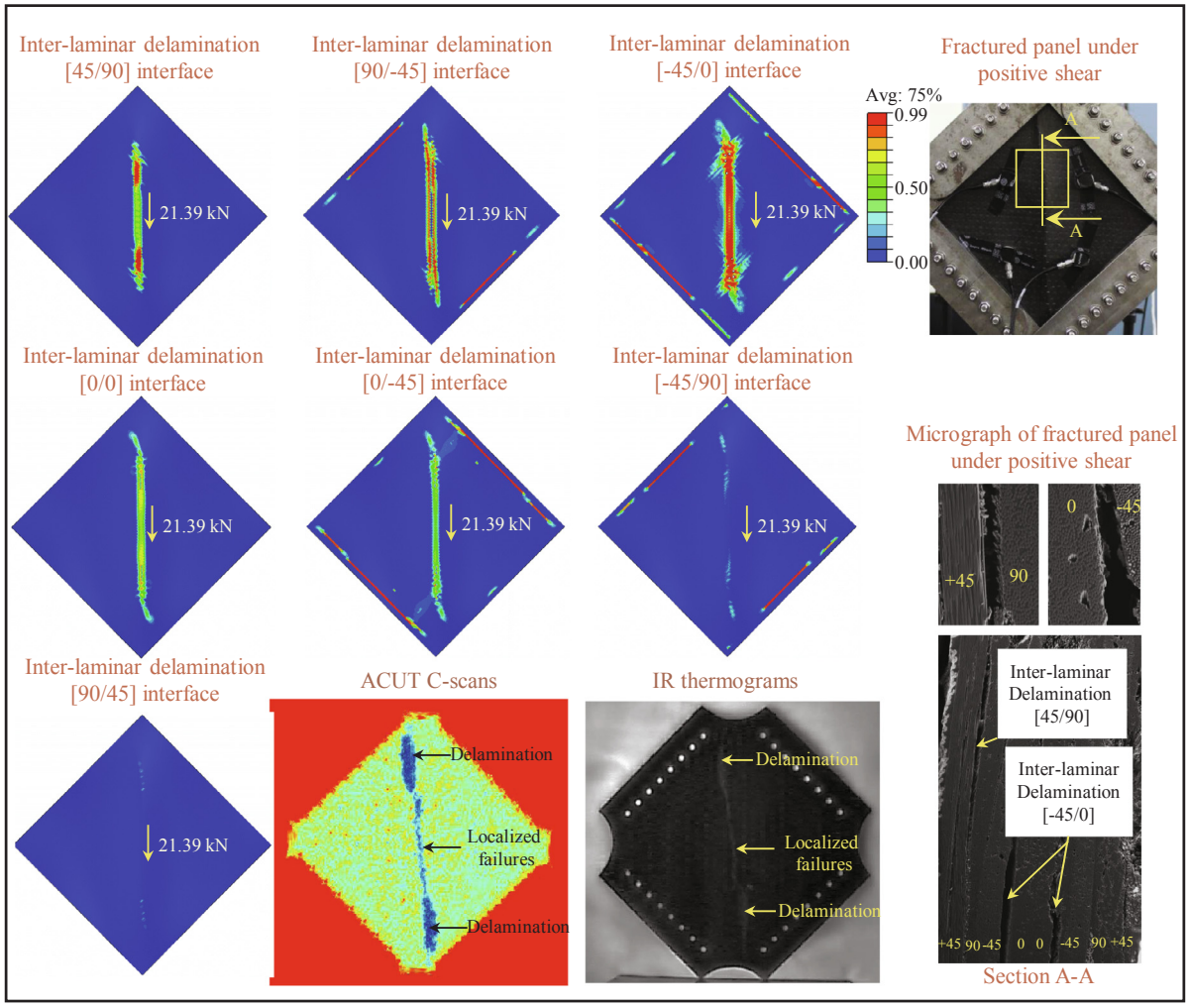

Fig. 21. Inter-laminar delamination failures captured by the PDM under positive shear load and supporting NDT, micrographic evidences.

laminar delamination failures (See Fig. 14 and 15). Further, it is evident from the cumulative energy plots that the delamination and fiber failure are the dominating failure modes. The AE events associated with the delamination propagation has less AE energy (few 100 Joules). However, the damage events corresponding to the fiber failure have very high AE energy of the order 10^7 to 10^9 Joules (See Fig. 15(a) and (b)).

In the case of positive shear, the damage evolved with the onset of delamination followed by few fiber failure events (See Fig. 15(a)). Further, an apparent plateau in the load response is observed, indicating the stable delamination propagation/migration phenomenon (See Fig. 15(a)), which is followed by the collapse of the panel. The damage events corresponding to the inter-laminar delaminations are predominant in positive shear when compared to the negative shear as seen from the Fig. 14(a) and (b). The primary damage mode under negative shear load involves both fiber kinking failure and delamination, which continued until the final collapse. As a result, a gradually decreasing load response is evident, as shown in Fig. 15. However, from the cumulative energy plots, it is evident that fiber kinking failure under compression is the dominant damage mode observed under negative shear load application.

Post-failure inspections of the test panels also reveal crucial damage signatures (See Fig. 16). Under positive shear load, the post-failure images depicted in Fig. 16(a) shows no significant damages on the outer plies. In the case of negative shear load, one can observe that the damage started as fiber–matrix shear failure in the outer 45° plies, followed by a fiber kinking failure under compression. Thus, it is evident from Fig. 16 that the test panel under positive shear fails along the loading direction and in the case of negative shear, the panel fails perpendicular to the loading direction.

4.1.3. Damage assessments obtained form NDT studies

ACUT and IPT techniques are utilized for assessing the damaged area within the failed CFRP test panels. The ACUT C-scan image of the fractured CFRP test panels is shown in Fig. 17(b). Under positive shear, the inter-laminar delamination damage is more predominant near the longitudinal corners of the test panel (See Fig. 17(b)). Later, the damage propagates within the test panel along the loading direction in the form of intra-laminar (fiber and matrix) failures. However, in the case of a negative shear load, the damage progress across the net section of the panel transverse to the loading direction. The damages are identified as localized delamination and fiber–matrix failures under compression. Further, the damage-maps acquired using the ACUT technique is supplemented with IPT measurements (See Fig. 17(c)). The thermograms obtained from the IPT technique also shows similar damage spread area and thus corroborates well with the ACUT scans of the CFRP panels.

Summary of the results obtained from the integrated experimental approach shows that the post-buckling performance of the test panels under positive and negative shear loads is successfully captured. The whole-field measurements obtained from the 3D-DIC system are useful in evaluating the buckling and post-buckling behavior. Also, the DIC measurements are supported by the strain gage data collected from the

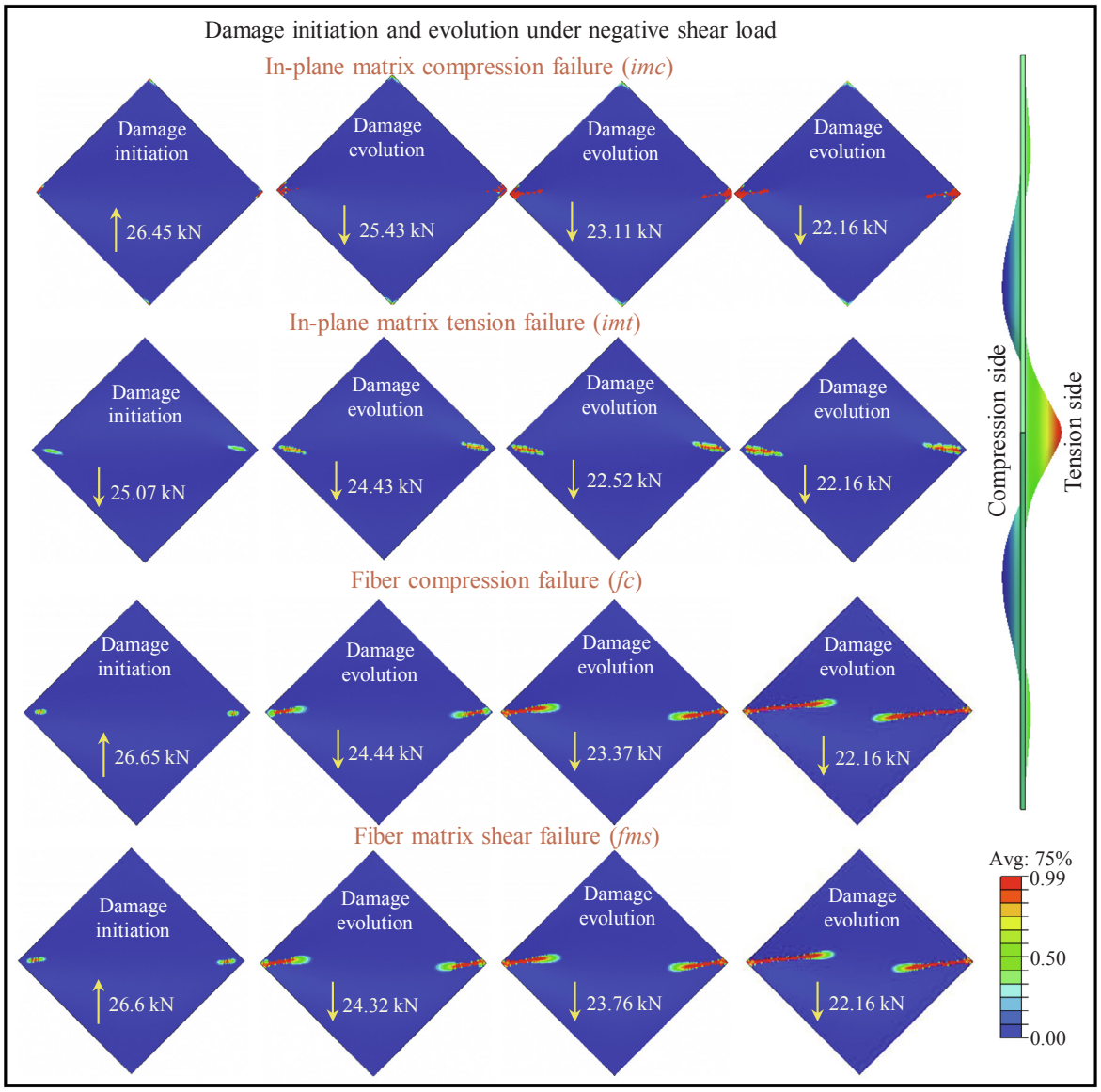

Fig. 22. Damage initiation and evolution simulated by the PDM under negative shear load.

critical locations in the test panel. The various damages exhibited by the test panel are assessed and classified using AE parametric data. Further, the damages are quantified by the post-test NDT assessments of the failed test panels. Therefore, the integrated experimental approach used in the current study provide insights into the post-buckling behavior and failure characteristics of the CFRP composite panels under in-plane shear loading.

4.2. Numerical results

In this section, the numerical results of post-buckling response and collapse behavior of CFRP test panels under in-plane shear evaluated by the PDM are presented. The computational time taken by the proposed damage model in case of the positive and negative shear buckling loading is 6.2 and 7.6 h, respectively, with a 16 CPU processor computer. The initiation and evolution of intra and inter-laminar damages under positive and negative shear loading are discussed in detail. Further, the damage evolution and associated damage mechanism results evaluated by the PDM are validated with the experimental observations. Moreover, the damage assessment data from the NDT and fractography studies is used to supplement the PDM predictions.

4.2.1. Comparison of FEA and experimental results

The deformation contours (in-plane and out-of-plane displacement) computed by the finite element model in the case of positive and negative shear loading are compared with the whole-field experimental 3D-DIC results, as shown in Fig. 18. For the positive shear case, the deformations contours correspond to a shear load of 19.89 kN, while for the negative shear load, they correspond to 25 kN. A good correlation between the numerical and experimental deformation maps is observed. Further, the post-buckling performance of the CFRP test panels under positive and negative shear load evaluated by the current numerical model (PDM in conjunction with CZM) are compared with the experimental results (See Fig. 19). The results show a good agreement with the experiments in terms of the pre-buckling and post-buckling stiffness. Also, the failure load and displacement computed by the PDM reasonably matches well with the experimental values. Under positive shear, the average collapse load obtained from experiments is 22.3 kN, whereas, from the FE model, evaluated to be 23.9 kN. However, in the case of negative shear, the average collapse load obtained from experiments and FE model are 27.2 kN and 26.73 kN, respectively.

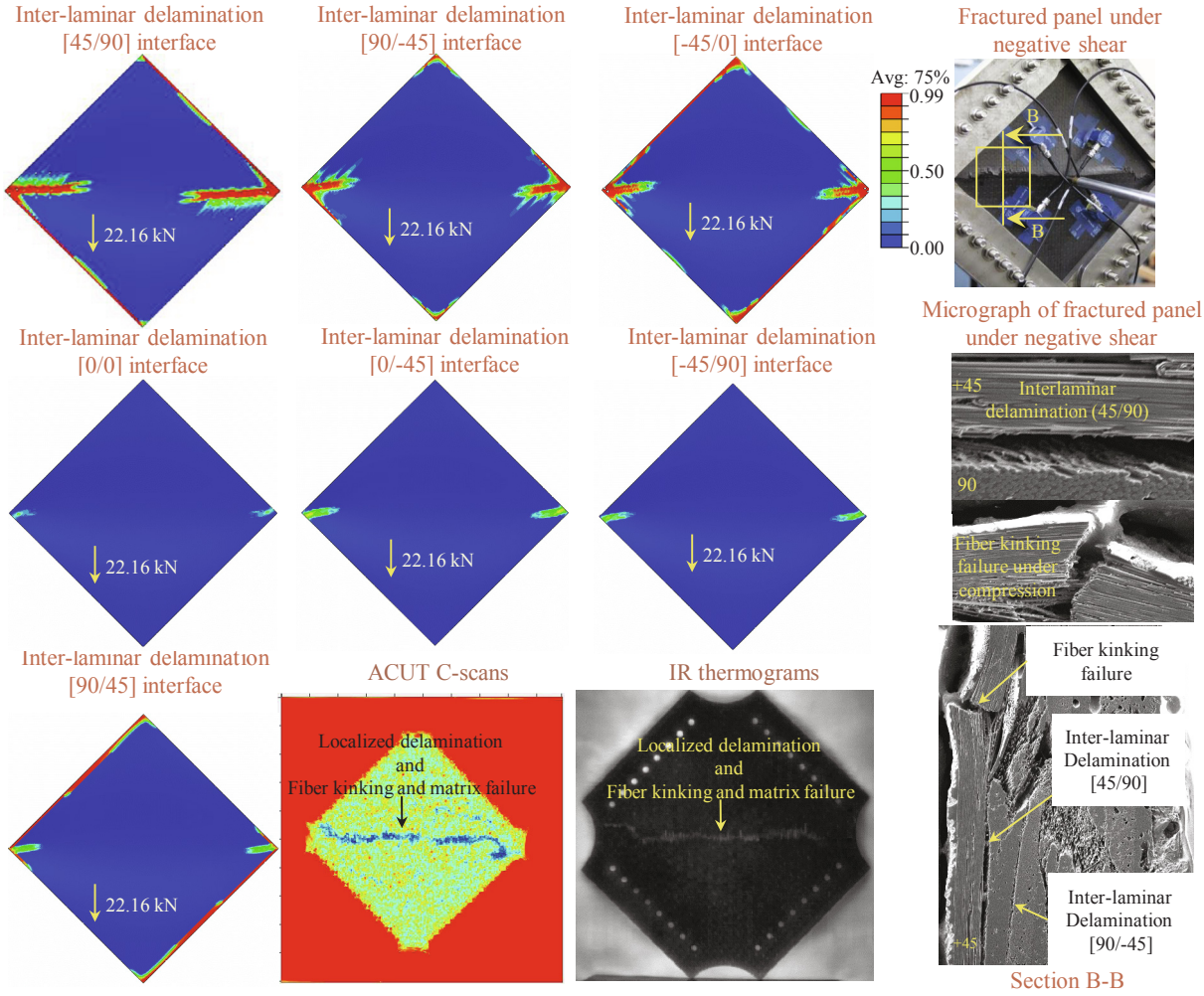

Fig. 23. Inter-laminar delamination failures captured by the PDM under negative shear load and supporting NDT, micrographic evidences.

4.2.2. Intra and inter-laminar damage predictions by PDM under positive shear

The transverse deformation of the laminate in the post-buckling regime results in in-plane matrix tension and compression failures are predominantly seen in the top and bottom plies, respectively (See Fig. 20). The bottom plies which are under tension have shown the matrix tensile failure, starting from the center of the panel at 19.5 kN. Whereas, the matrix compression failure is seen in the top plies near the corners at 21.53 kN load. The near-surface 45° plies, which are in line with the loading direction, show the evidence of fiber tension failure. Subsequently, with further increments in the load, the damage modes coalesced together and result in the ultimate failure of the panel. The damage is characterized by a fracture that progress along the loading direction with a gradual load drop, as shown in Fig. 20.

Inter-laminar delamination failures simulated by the FE model under positive shear load are shown in Fig. 21. It is observed that the test panels show local delamination failures along the loading direction. Delaminations are dominant at interfaces of the top layers (compression side) compared to the bottom layers (tension side). From the PDM predictions, one can observe that the delamination failures are prevalent as they approach the longitudinal corners. Further, the NDT and fractographic studies also support the damage predictions made by the FE model.

4.2.3. Intra and inter-laminar damage predictions by PDM under negative shear

In the case of negative shear load, the major dominant failure modes observed are fiber-matrix shear and fiber kinking (See Fig. 22). The top 45° ply, which is under direct compression, has shown the evidence of fiber kinking failure and fiber-matrix shear failure. Similar to the experiments, the damage in PDM also initiate (at ≈ 26.6 kN) at the transverse corners and progress across the panel net section. The matrix tension failure is observed in the bottom 45° plies and with loading, it traverses towards the center. The inter-laminar (delaminations) failures simulated by the PDM model are shown in Fig. 23. It shows that the delamination failures are confined only to the top layer interfaces similar to the positive shear load. It is also clear from the figure that the delamination is significant in the top [45/90] interface. Also, it is appreciable in the subsequent [90/-45] and [-45/0] layers. The damages assessed by the NDT methods and the post-failure micrographs of the fractured test panel ascertain the same failure mechanism and corroborates well with PDM results (See Fig. 22).

5. Conclusions

In this work, a detailed experimental and numerical study on the post-buckling response and failure of a quasi-isotropic CFRP test panel under in-plane shear loading is presented. An integrated experimental approach involving various on-line monitoring techniques are used for capturing the stability and failure characteristics of the CFRP test panels. Further, a generic FE based PDM is developed in Abaqus software to simulate the post-buckling response and collapse behavior of the test panels.

It is experimentally shown that the direction of the applied shear

load has got a major influence on the post-buckling characteristics and the associated failure mechanisms. The quasi-isotropic CFRP test panels have exhibited improved buckling and post-buckling performance under negative shear when compared to positive shear. It is attributed to the alignment of the compressive forces along the fiber direction by the applied shear load. Under positive shear load, the major damage modes observed are the intra-laminar matrix failures and the delamination. However, under negative shear load, fiber kinking and the fiber–matrix shear failure are predominantly observed. An experimental benchmark study has been shown for the first time, which would help us in further enhancing our understanding of damage evolution under in-plane shear loads. The complex failure mechanism is also captured by the proposed PDM, which supports the experimental findings. Therefore, the developed generic PDM model can be used for the design of the composite structures in the post-buckling regime and allows options to reduce the mass of the composite structure.

Declaration of Competing Interest

The authors declare that they have no known competing financial interests or personal relationships that could have appeared to influence the work reported in this paper.

Acknowledgment

The current research was partially supported by the Department of Science and Technology (DST) through the Fast Track Scheme for Young Scientists (Project No's: YSS/2014/000435, YSS/2015/000677). The authors would like to acknowledge JICA for funding the ACUT system and digital microscope used in this work. The authors are also grateful to the staff of Central Workshop IIT Hyderabad for their support and help in the manufacturing of test fixtures and panels.

References

[1] Kaminski B, Ashton J. Diagonal tension behavior of boron-epoxy shear panels. J Compos Mater 1971;5(4):553–8.
[2] Prabhakara M, Kennedy J. Nonlinear behaviour of unsymmetric, angle-ply, rectangular plates under in-plane edge shear. J Mech Eng Sci 1979;21(3):205–12.
[3] Agarwal B. Postbuckling behavior of composite shear webs. AIAA J 1981;19(7):933–9.
[4] Farley GL, Baker DJ. In-plane shear test of thin panels. Exp Mech 1983;23(1):81–8.
[5] Matthews F, Zhang Y. Postbuckling behavior of anisotropic laminated plates under pure shear and shear combined with compressive loading. AIAA J 1984;22(2):281–6.
[6] Kosteletos S. Postbuckling response of laminated plates under shear load. Compos Struct 1992;20(3):137–45.
[7] Leissa AW. A review of laminated composite plate buckling. Appl Mech Rev 1987;40(5):575–91.
[8] Nemeth MP. Buckling behavior of long symmetrically laminated plates subjected to combined loadings. Technical Paper 3195, NASA; 1992.
[9] Nemeth MP. Buckling behavior of long symmetrically laminated plates subjected to shear and linearly varying axial edge loads. Technical Paper 3659, NASA; 1997.
[10] Singh S, Kumar A. Postbuckling response and failure of symmetric laminates under in-plane shear. Compos Sci Technol 1998;58(12):1949–60.
[11] Loughlan J. The influence of bend-twist coupling on the shear buckling response of thin laminated composite plates. Thin-walled Struct 1999;34(2):97–114.
[12] Jha PN, Kumar A. Response and failure of square laminates under combined loads. Compos Struct 2002;55(3):337–45.
[13] Iyengar N, Chakraborty A. Study of interaction curves for composite laminate subjected to in-plane uniaxial and shear loadings. Compos Struct 2004;64(3–4):307–15.
[14] Featherston CA, Watson A. Buckling of optimised flat composite plates under shear and in-plane bending. Compos Sci Technol 2005;65(6):839–53.
[15] Mallela UK, Upadhyay A. Buckling of laminated composite stiffened panels subjected to in-plane shear: a parametric study. Thin-walled Struct 2006;44(3):354–61.
[16] Jung W-Y, Han S-C. Shear buckling responses of laminated composite shells using a modified 8-node ANS shell element. Compos Struct 2014;109:119–29.
[17] Chen Q, Qiao P. Shear buckling of rotationally-restrained composite laminated plates. Thin-Walled Struct 2015;94:147–54.
[18] Kumar D, Singh S. Effects of boundary conditions on buckling and postbuckling responses of composite laminate with various shaped cutouts. Compos Struct 2010;92(3):769–79.
[19] Kumar D, Singh S. Postbuckling strengths of composite laminate with various shaped cutouts under in-plane shear. Compos Struct 2010;92(12):2966–78.
[20] Kumar D, Singh S. Stability and failure of composite laminates with various shaped cutouts under combined in-plane loads. Compos Part B: Eng 2012;43(2):142–9.
[21] Kumar D, Singh S. Effects of flexural boundary conditions on failure and stability of composite laminate with cutouts under combined in-plane loads. Compos Part B: Eng 2013;45(1):657–65.
[22] Raju G, Wu Z, Weaver PM. Buckling and postbuckling of variable angle tow composite plates under in-plane shear loading. Int J Solids Struct 2015;58:270–87.
[23] Li X, Gao W, Liu W. Post-buckling progressive damage of CFRP laminates with a large-sized elliptical cutout subjected to shear loading. Compos Struct 2015;128:313–21.
[24] Lei Z, Bai R, Tao W, Wei X, Leng R. Optical measurement on dynamic buckling behavior of stiffened composite panels under in-plane shear. Opt Lasers Eng 2016;87:111–9.
[25] Li X, Gao W, Liu W. The bearing behavior and failure characteristic of CFRP laminate with cutout under shearing load: Part I. Exp, Compos Struct 2016;141:355–65.
[26] Ge D, Mo Y, He B, Wu Y, Du X. Experimental and numerical investigation of stiffened composite curved panel under shear and in-plane bending. Compos Struct 2016;137:185–95.
[27] Kolanu NR, Prakash SS, Ramji M. Experimental study on compressive behavior of GFRP stiffened panels using digital image correlation. Ocean Eng 2016;114:290–302.
[28] Dávila CG, Bisagni C. Fatigue life and damage tolerance of postbuckled composite stiffened structures with initial delamination. Compos Struct 2017;161:73–84.
[29] Gutkin R, Green C, Vangrattanachai S, Pinho S, Robinson P, Curtis P. On acoustic emission for failure investigation in CFRP: Pattern recognition and peak frequency analyses. Mech Syst Signal Process 2011;25(4):1393–407.
[30] Ono K, Gallego A. Research and applications of AE on advanced composites. J Acoust Emiss 2012;30:180–229.
[31] Aggelis D, Barkoula N-M, Matikas T, Paipetis A. Acoustic structural health monitoring of composite materials: damage identification and evaluation in cross ply laminates using acoustic emission and ultrasonics. Compos Sci Technol 2012;72(10):1127–33.
[32] Masmoudi S, El Mahi A, Turki S. Use of piezoelectric as acoustic emission sensor for in situ monitoring of composite structures. Compos Part B: Eng 2015;80:307–20.
[33] Mohammadi R, Najafabadi MA, Saeedifar M, Yousefi J, Minak G. Correlation of acoustic emission with finite element predicted damages in open-hole tensile laminated composites. Compos Part B: Eng 2017;108:427–35.
[34] Saidane EH, Scida D, Assarar M, Ayad R. Damage mechanisms assessment of hybrid flax-glass fibre composites using acoustic emission. Compos Struct 2017;174:1–11.
[35] Kolanu NR, Raju G, Ramji M. Damage assessment studies in CFRP composite laminate with cut-out subjected to in-plane shear loading. Compos Part B: Eng 2019;166:257–71.
[36] Catalanotti G. Prediction of in situ strengths in composites: Some considerations. Compos Struct 2019;207:889–93.
[37] Kolanu NR, Raju G, Ramji M. Experimental and numerical studies on the buckling and post-buckling behavior of single blade-stiffened CFRP panels. Compos Struct 2018;196:135–54.
[38] Yang Y, Liu X, Wang Y-Q, Gao H, Li R, Bao Y. A progressive damage model for predicting damage evolution of laminated composites subjected to three-point bending. Compos Sci Technol 2017;151:85–93.
[39] ABAQUS/Standard User's Manual, Version 2017, Simulia; 2016.
[40] Benzeggagh ML, Kenane M. Measurement of mixed-mode delamination fracture toughness of unidirectional glass/epoxy composites with mixed-mode bending apparatus. Compos Sci Technol 1996;56(4):439–49.
[41] Sobhith K. Study of Delamination, Matrix/fiber damage in CFRP under bending using Acoustic Emission and Cohesive Zone technique. Indian Institute of Technology Hyderabad; 2017.